Molecular Beam Scattering from Flat Jets of Liquid Dodecane and Water

Walt Yang[1,2], *Madison M. Foreman*[1,2], *Steven Saric*[1,2], *Alec M. Wodtke*[3], *Kevin R. Wilson*[2], *Daniel M. Neumark*[1,2,*]

[1] *Department of Chemistry, University of California, Berkeley, CA 94720, USA*

[2] *Chemical Sciences Division, Lawrence Berkeley National Laboratory, Berkeley, CA 94720, USA*

[3] *Department of Dynamics at Surfaces, Max Planck Institute for Multidisciplinary Sciences, am Faßberg 11, 37077 Göttingen, Germany*

[*] **Author to whom correspondence should be addressed: dneumark@berkeley.edu**

ABSTRACT

Molecular beam experiments in which gas molecules are scattered from liquids provide detailed, microscopic perspectives on the gas–liquid interface. Extending these methods to volatile liquids while maintaining the ability to measure product energy and angular distributions presents a significant challenge. The incorporation of flat liquid jets into molecular beam scattering experiments in our laboratory has allowed us to demonstrate their utility in uncovering dynamics in this complex chemical environment. Here, we summarize recent work on the evaporation and scattering of Ne, CD_4, ND_3, and D_2O from a dodecane flat liquid jet and present first results on the evaporation and scattering of Ar from a cold salty water jet. In the evaporation experiments, Maxwell–Boltzmann flux distributions with a $\cos\theta$ angular distribution are observed. Scattering experiments reveal both impulsive scattering and trapping followed by thermal desorption. Super-specular scattering is observed for all four species scattered from dodecane and is attributed to anisotropic momentum transfer to the liquid surface. In the impulsive scattering channel, rotational excitation of the polyatomic scatterers is a significant energy sink, and these species accommodate more readily on the dodecane surface compared to Ne. Our preliminary results on cold salty water jets suggest that Ar atoms undergo vapor-phase collisions when evaporating from the liquid surface. Initial scattering experiments characterize the mechanisms of Ar interacting with an aqueous jet, allowing for comparison to dodecane systems.

Key Points

- Molecular beam scattering from flat liquid jets is a powerful technique to elucidate mechanistic detail at the gas–liquid interface.
- Previous dodecane scattering experiments have uncovered angularly-resolved TD fractions and energy transfer at the interface for several small molecule scatterers.
- Preliminary results on scattering from cold salty water reveal mechanisms of interaction between argon and an aqueous jet.

KEYWORDS

Water interface, flat liquid jets, molecular beam scattering, interfacial dynamics, energy transfer, kinematic modeling

I. INTRODUCTION

The gas–liquid interface is a chemical environment that governs many key processes essential for everyday life. Notable examples include the adsorption of O_2 and the desorption of CO_2 at the air–lung interface,[1,2] controlling air–fuel mixing in internal combustion engines[3] and the treatment of amine gases,[4] and the formation of acid rain and modulation of atmospheric ozone.[5-9] Extracting information on molecular-level structure, kinetics, and dynamics at the gas–liquid interface requires methods specifically geared toward surface studies.[10-12] Novel spectroscopic and kinetics techniques have been developed to address this challenge.[13-15] Deep ultraviolet electronic sum frequency generation spectroscopy has revealed charge-transfer-to-solvent transitions in anions at the air–water interface[16-19] and vibrational spectroscopy has been used to interrogate formic acid orientation with angstrom-level depth resolution.[20] Additionally, thin film and microdroplet studies have uncovered augmented chemical reaction rates compared to their bulk counterparts.[21-24] This paper focuses on molecular beam experiments that probe the gas–liquid interface.

Fundamental interactions between particles in the gas and liquid phases underlie both structural characteristics and dynamical phenomena at the interface. Molecular beam scattering experiments offer an effective means of probing these interactions, building on the knowledge developed through molecular beam scattering from solid surfaces to probe nonreactive[25-28] and reactive[27,29] processes. Enabled by developments of the liquid microjet by Faubel[30-32] and the wetted wheel by Fenn[33] and Siegbahn,[34] Nathanson, Minton, and others have paved the way for molecular beam experiments on the gas–liquid interface.[35-44] These experiments have elucidated an unprecedented level of mechanistic detail behind gas–liquid interactions.[45,46]

The advent of microfluidic chips that generate flat liquid jets[47] led us to perform angle-resolved molecular beam scattering experiments on the vacuum–dodecane interface. In this paper, we highlight our previous results[48-50] scattering select species from a dodecane flat liquid jet, where we compared how the dodecane surface differs from other hydrocarbon surfaces such as squalane.[35,51] We also present new

results on the evaporation and scattering of Ar from a cold salty water jet. The experiments performed in our group show how molecular beam scattering coupled with flat liquid jets provides a powerful approach to understanding interfacial behavior.

Evaporation and scattering experiments require maintaining a clean liquid surface and, to be compatible with a vacuum environment, the chosen liquids must have a low vapor pressure to minimize the contribution of collisions with the vapor jacket surrounding the surface of the jet. The flat liquid jet satisfies these conditions by introducing a continuously flowing liquid into the vacuum chamber as well as granting access to more volatile solvents than those compatible with the wetted wheel approach (*cf.* $\sim 10^{-2}$ and $< 10^{-3}$ Torr, respectively). Compared to cylindrical jets, a flat jet offers a larger target ($\sim$1 mm versus $\sim$30 μm) for molecular beam scattering, leading to substantially higher scattering signal. Additionally, a flat jet has a well-defined surface normal, thereby enabling angularly-resolved measurements.[46]

In our prior work on dodecane flat jets ($P_{vap} = 1.5 \times 10^{-2}$ Torr at 275 K), we characterized the liquid interface by measuring the angular and translational energy distributions of Ne, CD_4, ND_3, and D_2O evaporating and scattering from dodecane.[48-50] Through evaporation of these species from the jet, we deduced that conditions were present for nascent scattering to take place. We then considered two limiting nonreactive scattering mechanisms at the gas–liquid interface. Impulsive scattering (IS) arises when incident gas molecules undergo inelastic collisions with the surface, while thermal desorption (TD) takes place when trapping leads to residence times at the surface that are long enough for thermalization.[26,45] Based on previous angularly-resolved measurements, the IS pathway is expected to lead to specular scattering, or detection of scattered particles at angles determined by the initial energy and incident trajectory, whereas TD yields $\cos\theta$ angular distributions with respect to the surface normal.[26,52] Note that while the simple partitioning between IS and TD is a useful framework for interpreting experimental observations, in reality scattering is a much more complicated process.[53]

In our prior scattering experiments, we examined the partitioning between these two mechanistic pathways and found that interfacial behavior is largely dictated by scatterer identity. We also measured TD fractions and the degree of energy transfer in the IS channel at multiple deflection angles. Super-specular scattering was observed for all four scatterers. We compared our findings to those of Saecker and Nathanson, where Ne, CH_4, D_2O, and NH_3 were scattered from a squalane ($P_{vap} = 10^{-7}$ Torr at 295 K) wetted wheel at a single deflection angle.[51] In that same study, a glycerol surface was also interrogated, and it was found that squalane presents a rougher and softer surface than glycerol, leading to a higher likelihood of trapping scatterers at the interface.

More complex and volatile liquids have been studied since, such as surfactant-coated NaBr/glycerol,[41,43] concentrated aqueous LiBr and LiCl solutions,[38,40] and surfactant-coated aqueous LiBr solutions.[54] Studies on these aqueous systems have been crucial in understanding the air–water interface at a fundamental level but are limited by the usage of cylindrical microjets which do not provide angular resolution. Thus, we demonstrate the first angularly-resolved experiments reporting mechanistic detail at the gas–water interface through the evaporation and scattering of Ar from a cold aqueous 8 molal LiBr flat jet ($P_{vap} = 5.2 \times 10^{-2}$ Torr at 225 K). Preliminary results show that evaporation of Ar from the jet can be well-described by a Maxwell–Boltzmann flux distribution. Additionally, TD fractions at select scattering angles suggest that cold salty water is a more accommodating surface than dodecane for rare gases. Given the angular specificity of the flat liquid jet and that the deflection angle can alter mechanistic partitioning so drastically, these first results lay the foundation for investigating angular-dependent reactivity at the water surface.

II. EXPERIMENTAL APPARATUS

All experiments are performed in a crossed molecular beam instrument[55,56] adapted for gas–liquid scattering as described in detail previously.[48] The apparatus comprises three vacuum chambers housing the pulsed molecular beam source, collision region, and rotatable detector, all evacuated by turbomolecular pumps.

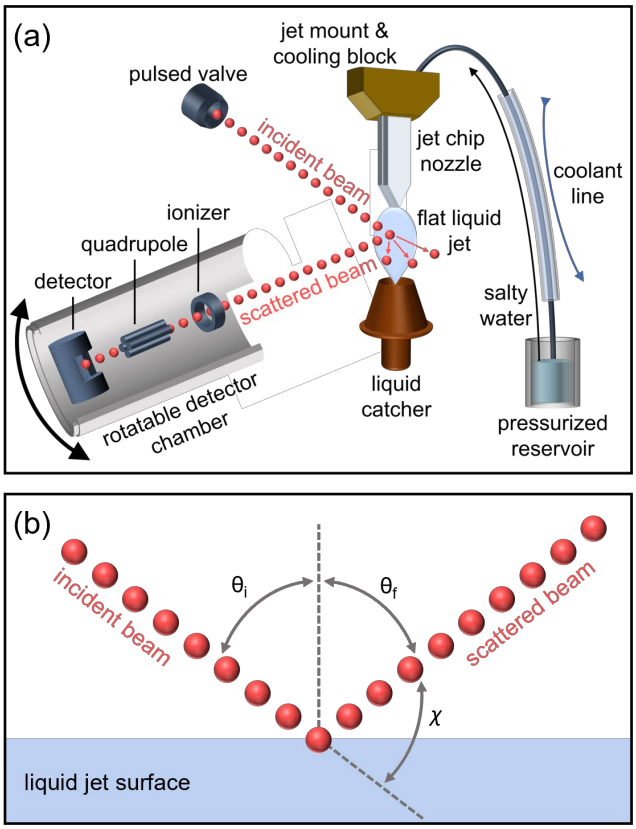

Figure 1. (a) Schematic diagram of the scattering setup for a cold salty water jet. All components are situated inside the collision chamber (not shown). (b) Definition of the incidence angle θ_i, scattering angle θ_f, and deflection angle $\chi = 180° - (\theta_i + \theta_f)$.

A schematic diagram of the entire scattering setup is shown in Fig. 1. The pulsed molecular beam is generated within the source chamber and interacts with the flat liquid jet in the collision chamber. A large-area, liquid nitrogen-cooled copper wall within the scattering chamber yields a very high pumping speed for vapor from the jet. Scattered products then enter the triply-differentially pumped rotatable detector chamber that comprises an electron impact ionizer (80 eV electron kinetic energy), quadrupole mass filter, and ion detection assembly. Fig. 1 defines the incidence angle θ_i, scattering angle θ_f, and deflection angle $\chi = 180° - (\theta_i + \theta_f)$. For the dodecane studies, θ_i is chosen to be 45, 60, or 80°, enabled by rotation of the chip holder. Due to geometrical constraints of the scattering apparatus, outgoing angles θ_f are restricted to a range between $90° - \theta_i$ and 90°. For scattering from salty water, θ_i is chosen to be 60°.

As in prior work, a piezoelectric valve (MassSpecpecD BV, Enschede)[57,58] generates the pulsed molecular beams used herein. Ne, CD_4, ND_3, and D_2O supersonic beams are seeded in helium at respective

compositions of 10, 0.75, 1.5, and ~0.5 %.[49,50] The Ar beam is prepared similarly by seeding ~10 % Ar in He, and stagnation conditions are typically 293 K and 3000 Torr. Note that a dimer ratio of 5 % is present for D_2O, but no dimers were detected for either CD_4 or ND_3. The velocities of the molecular beams are characterized by time-of-flight (TOF) measurements with a rotating (200 Hz) chopper wheel (two slits, 14 μs open time). This results in beam velocities of 1562 ± 165, 1732 ± 185, 1730 ± 205, 1791 ± 347, and 1454 ± 208 m s^{-1} (FWHM), with mean translational energies of 23.7, 29.3, 28.8, 33.4, and 41.5 kJ mol^{-1} for Ne, CD_4, ND_3, D_2O, and Ar, respectively.

Within the collision chamber, flat liquid jets are formed using a microfluidic chip.[47] As described previously for the dodecane jet, an HPLC pump is employed to deliver the solvent through a pre-cooling stage to the jet nozzle at a flow rate of 3.5 mL min^{-1} and a flow velocity of 10 m s^{-1}, leading to a detector viewing time of ~600 μs. Typical dimensions of the first flat jet sheet are 1.5 × 4.5 mm^2 (W × H) with a thickness estimated to be ~1.5 μm at its center.[32] For the cold salty water jet, a 2.3 L glass cylinder containing 8 m LiBr dissolved in H_2O (Milli-Q®, MilliporeSigma) is housed in a pressurized stainless steel reservoir. To operate the jet at a flow rate of ~2 mL min^{-1} at a temperature of ~226 K at the jet nozzle, the reservoir is pressurized to 85 bar. This leads to a flow velocity of 7 m s^{-1} and a detector viewing time of ~500 μs (~4 mm at the interaction region with the detector gate valve opened to a 2 mm circular aperture).

For the dodecane jet, a stainless-steel chip holder is used and the temperature of the jet is determined through evaporation TOF characterization, similar to argon thermometry.[46] This results in liquid temperatures T_{liq} of 283, 273, 269, and 274 K for dodecane doped with Ne, CD_4, ND_3, and D_2O, respectively, for the evaporation experiments. T_{liq} = 269 K for all dodecane scattering experiments. The temperature gradient across the jet surface is expected to be small due to the high isobaric heat capacity and low vapor pressure of dodecane, suppressing evaporative cooling effects.[59,60] The samples were prepared through a process that has been described previously for Ne, CD_4, ND_3, and D_2O in dodecane

150 (n-$C_{12}H_{26}$, TCI America #D0968).[48-50] For the scattering experiments, pure dodecane is used after
151 vacuum-degassing with pure He.

152 Multiple modifications have been implemented to operate a cold salty water jet. Marine-grade 464 brass
153 rather than stainless steel is used for part of the chip holder assembly due to its increased corrosion
154 resistance. To achieve significantly lower jet temperatures, a commercial marine utility pump (Xylem
155 Rule iL280P) circulates an ethanol bath held at 233 K through an in-line stainless-steel counter-current
156 pre-cooling stage that surrounds the solvent delivery line. The salty water flows through this stage for ~1
157 m prior to entering the collision chamber. For additional cooling, flexible Cu braids are attached to a solid
158 Cu extrusion from the cryogenically cooled Cu wall inside of the collision chamber. These braids connect
159 to the chip holder with temperature T_{holder} recorded by a thermocouple. The temperature difference
160 $T_{\mathrm{holder}} - T_{\mathrm{liq}}$ is estimated to be less than 3 °C for the salty water jet due to its relatively low vapor
161 pressure.[40,46] For both evaporation and scattering experiments, T_{holder} was measured to be 226 K. The salty
162 water sample is prepared by dissolving Ar in 8 m aqueous LiBr by vacuum-degassing the liquid. For
163 scattering from salty water, 8 m LiBr is used after vacuum-degassing with pure N_2.

164 The translational energy distribution of evaporated and scattered species is determined by time-of-flight
165 (TOF) measurements. In the evaporation experiments, time zero is set by the chopper wheel positioned
166 between the jet and the detector. Detector angles θ_f range from 0 to 90° with respect to the surface normal.
167 In scattering experiments, the chopper wheel is translated away from the detector axis, and the moment
168 when the most intense part of the pulsed molecular beam reaches the interaction region defines time zero
169 at the interaction region. As a result, the temporal resolution of the scattering TOF measurements is limited
170 by the quality of the pulsed beam profiles. For Ne, CD_4, ND_3, D_2O, and Ar, the valve opening time is set
171 to 15, 15, 12, 30, and 13 μs, respectively. Temporal widths measured at the detector were 28, 26, 27, 43,
172 and 40 μs, respectively. The "beam-off" data is subtracted from "beam-on" data to achieve background-
173 subtracted scattering spectra. To ensure that systematic error is limited throughout, angular distributions
174 are measured in a back-and-forth matter as described prior.[48-50] Acquisition times for dodecane are

typically between 5 and 10 minutes for a single spectrum, while this is extended to 20 minutes for salty water.

III. RESULTS OF EVAPORATION EXPERIMENTS ON DODECANE

To isolate TD and determine that conditions for nascent scattering exist, evaporation TOF spectra were taken for doped dodecane jets. Ne, CD_4, ND_3, and D_2O evaporation from their respective doped dodecane jets are shown in Fig. 2(a–c) for $\theta_f = 0$, 30, and 60°. Since these solutes are at thermal equilibrium with the liquid surface prior to evaporation, the product flux f can be described by a Maxwell–Boltzmann (MB) flux distribution[61]

$$f_{\mathrm{MB}}(v) \propto S_0(v,\theta)\, v^3 \exp\left(-\frac{mv^2}{2RT_{liq}}\right) \tag{1}$$

where v and m are the velocity and molecular mass of the evaporating molecule and R is the universal gas constant. $S_0(v,\theta)$ is the velocity- and angle-dependent sticking coefficient.

At $\theta_f = 0°$, Maxwellian behavior of the evaporating particles is observed; as θ_f approaches 60°, the TOF profiles for all four species broaden toward longer arrival times. This broadening, or sub-Maxwellian behavior, is from an isotropic background due to molecular desorption from the cryogenically cooled Cu wall that persists even if the jet is moved out of the viewing angle of the detector.[49,50,62] Thus, the TOF spectra are fitted by a linear combination of MB distributions at T_{liq} and T_{bkg}.

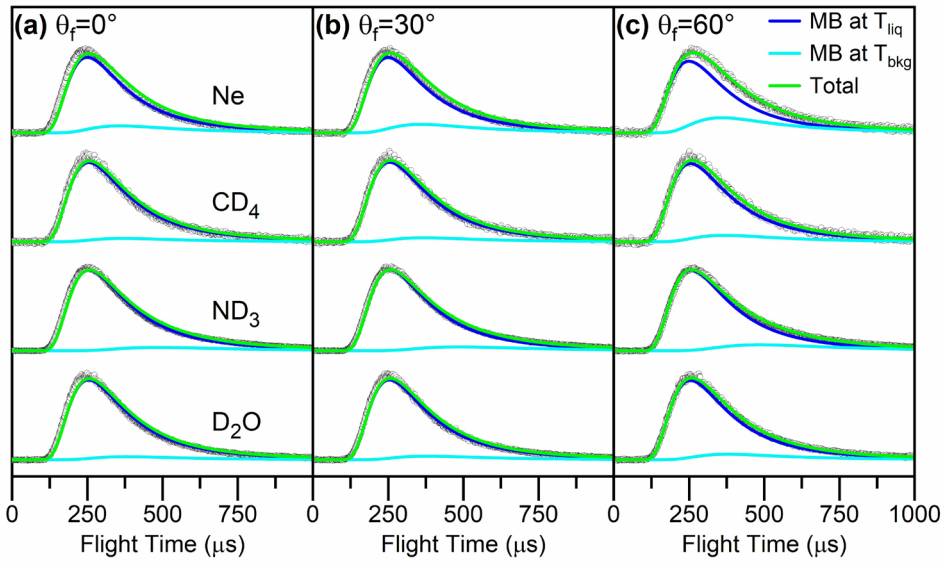

Figure 2. Normalized evaporation TOF spectra of Ne, CD_4, ND_3, and D_2O from doped liquid dodecane flat jets at (a) $\theta_f = 0°$, (b) $\theta_f = 30°$, and (c) $\theta_f = 60°$. TOF distributions are fitted with a combination of Maxwell–Boltzmann velocity distributions at $T_{liq} = 283$, 273, 269, and 274 K (blue traces) and at $T_{bkg} = 137$, 131, 75, and 123 K (light blue traces), respectively. The absolute intensity of the T_{bkg} component is kept constant for all angles. The sum of the two contributions is shown by the green traces.

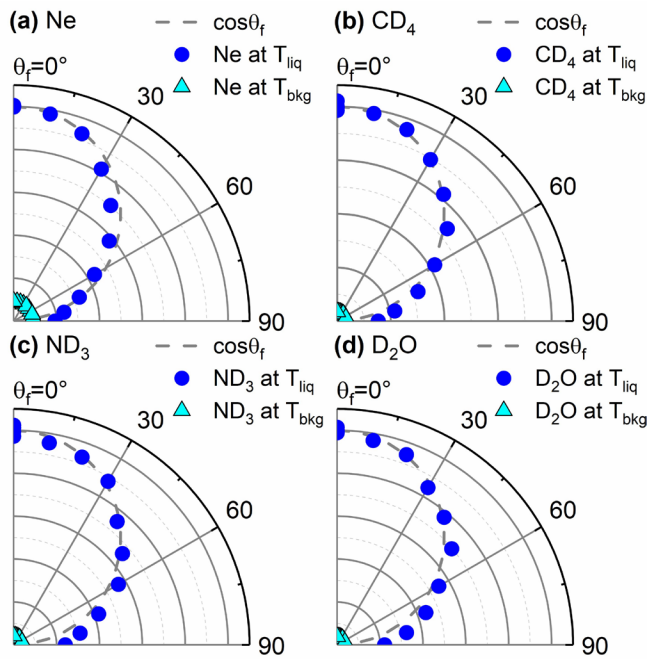

Figure 3. Angular plots created from the integrated, non-normalized intensities of the Maxwell–Boltzmann simulations at T_{liq} and T_{bkg} (blue circles and cyan triangles, respectively) of (a) Ne, (b) CD_4, (c) ND_3, and (d) D_2O evaporation data at various detector angles. The cosine function representing the expected angular distribution for evaporation is indicated by the dashed gray curve.

Integrating the fitted TOF spectra results in angular distributions where the total evaporative flux is plotted as a function of θ_f in Fig. 3 for Ne, CD_4, ND_3, and D_2O. As expected for an evaporative process

from a flat surface and provided that detailed balance holds,[61,63] the contributions at T_{liq} follow a $\cos\theta_f$ distribution.[64,65] Given that all four species exhibit both Maxwellian translational energy distributions and $\cos\theta_f$ angular distributions after accounting for background signal, our results indicate that the sticking coefficient $S_0(v,\theta)$ in Eq. 1 can be assumed to be unity[61] and that the evaporating species do not interact measurably with the vapor sheath around the jet. The latter observation implies that vapor sheath interactions will also be insignificant in scattering experiments.

IV. RESULTS OF SCATTERING EXPERIMENTS ON DODECANE

TOF spectra of Ne, CD_4, ND_3, and D_2O scattered from a dodecane jet are shown in Fig. 4(a–c) for $\theta_i = 60°$ and detector angles $\theta_f = 30$, 60, and 80°. Overall, comparing TOF profiles at the same θ_f reveals faster arrival times and narrower TOF distributions for scattered Ne compared to the polyatomic scatterers. The polyatomic scatterers behave similarly with only slight differences in the scattering profiles, though the ND_3 and D_2O distributions extend to longer arrival times compared to CD_4. As θ_f increases, the TOF profiles shift toward earlier arrival times. This trend is also observed for incidence angles of 45 and 80°.

The TOF distributions are fitted using two contributions—one assigned to a faster component from IS and the other a slower one from TD. The IS component is fitted to the flux distribution for a supersonic (SS) molecular beam in Eq. 2[66,67]

$$f_{SS}(v) \propto v^3 \exp\left(-\frac{m(v-v_{SS})^2}{2RT_{SS}}\right) \tag{2}$$

with average flow velocity v_{SS} and average temperature T_{SS}. The fits to the TOF spectra with a linear combination of SS and MB distributions representing the two scattering channels are also shown in Fig. 4.[45,68] Note that the fitting procedure involves convolution with the full molecular beam temporal profiles.

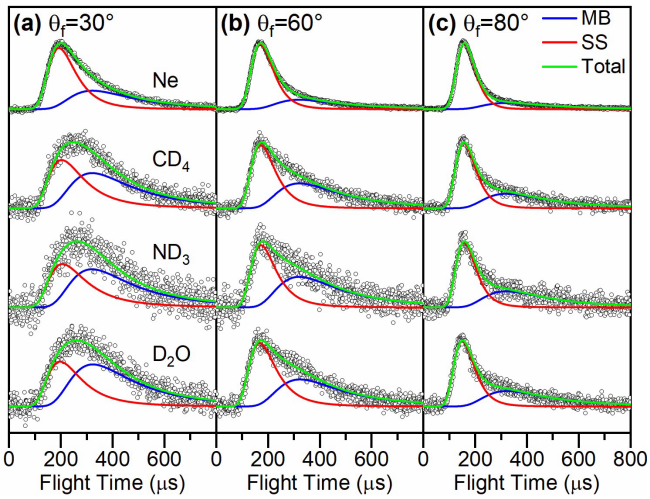

Figure 4. Normalized TOF spectra of Ne, CD_4, ND_3, and D_2O scattering from a dodecane flat jet with $\theta_i = 60°$ at (a) $\theta_f = 30°$, (b) $\theta_f = 60°$, and (c) $\theta_f = 80°$. The data are fitted by the sum (green traces) of an SS distribution (red traces) and an MB distribution (blue traces) at the liquid jet temperature. Mean translational energies E_i for Ne, CD_4, ND_3, and D_2O are 23.7, 29.3, 28.8, and 33.4 kJ mol^{-1}, respectively.

For all four species, the TD contribution drops as θ_f increases, resulting in narrower, faster TOF spectra. This result reflects the $\cos\theta_f$ angular distribution for TD, leading to less TD at higher θ_f. From the fitted TOF profiles, the polyatomic scatterers exhibit considerably more TD than Ne, especially at values of θ_f approaching the surface normal. It is also observed that the TD fractions for Ne are smaller than those for the polyatomic scatterers at all deflection angles. The TD fractions for the polyatomic species are similar, but overall, the trend manifests as Ne < CD_4 < D_2O < ND_3. This trend is discussed in more detail in Section IVb.

Angular distributions from integrating the fitted TOF profiles are shown in Fig. 5(a–d) for the four scatterers at $\theta_i = 60°$. For the TD channel, the integrated intensities closely follow a $\cos\theta_f$ angular distribution, consistent with our evaporation results, indicating that these particles have equilibrated at T_{liq} prior to desorbing. Although one might expect to observe specular scattering in the angular distributions of the IS channel, we observe super-specular scattering for all four systems, where the maximum IS intensity is found at $\theta_f > \theta_i$; for these systems, the angular distribution peaks at $\theta_f = 70°$. This result is attributed to collisions that favor momentum transfer along the surface normal.[69,70]

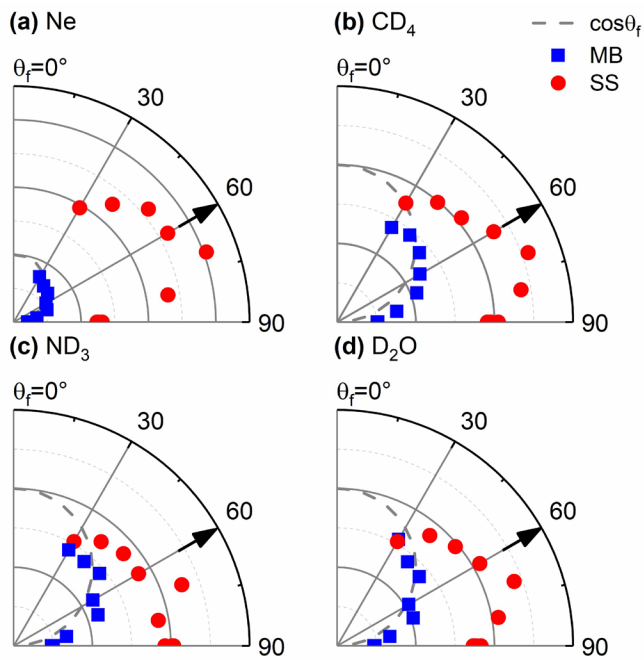

Figure 5. Angular plots created from the integrated, non-normalized intensities of scattering at $\theta_i = 60°$ for (a) Ne, (b) CD_4, and (c) ND_3, and (d) D_2O. Blue squares represent the TD (MB distribution) and red circles the IS (SS distribution) contributions to the TOF fits. The cosine function representing the expected angular distribution for evaporation is indicated by the dashed, gray curve. Arrows indicate the specular angle.

IVa. DISCUSSION OF IMPULSIVE SCATTERING FROM DODECANE

The scattering TOF profiles provide energetic information in the form of changes to the translational energies of the scattered molecular beams. Specifically, analyzing the IS channel within the scattering TOF profiles through established kinematic models reveals key findings on energy transfer at the gas–liquid interface. The soft-sphere kinematic model, previously applied to other scattering studies,[71,72] describes the average fractional energy loss as a function of deflection angle. The model is given by Eq. 3: [71,73,74]

$$\left(\frac{\Delta E}{E_i}\right) \approx \frac{2\mu}{(1+\mu)^2}\left[1+\mu(\sin\chi)^2-\cos\chi\sqrt{1-\mu^2(\sin\chi)^2-\frac{E_{int}}{E_i}(\mu+1)}+\frac{E_{int}}{E_i}\left(\frac{\mu+1}{2\mu}\right)\right]\left[1+\frac{V-2RT_{liq}}{E_i}\right] \quad (3).$$

where the absolute change in translational energy is $\Delta E = E_i - \langle E_{IS}\rangle$, with incident translational energy E_i and average energy in the IS channel $\langle E_{IS}\rangle$. The mass ratio $\mu = m_{gas}/m_{eff}$ between the gas molecule and the effective surface mass, the total internal excitation of both the scatterer and surface E_{int}, the liquid temperature T_{liq}, and the well depth of the gas–surface interaction potential V are also included. The

scattering geometry is represented by the deflection angle $\chi = 180° - (\theta_i + \theta_f)$. In essence, this is a modified line-of-centers model where internal excitation is allowed. The V/E_i and $-2RT_{liq}/E_i$ terms account for the effects of the interaction potential and thermal surface motions on $\Delta E/E_i$, respectively.[74]

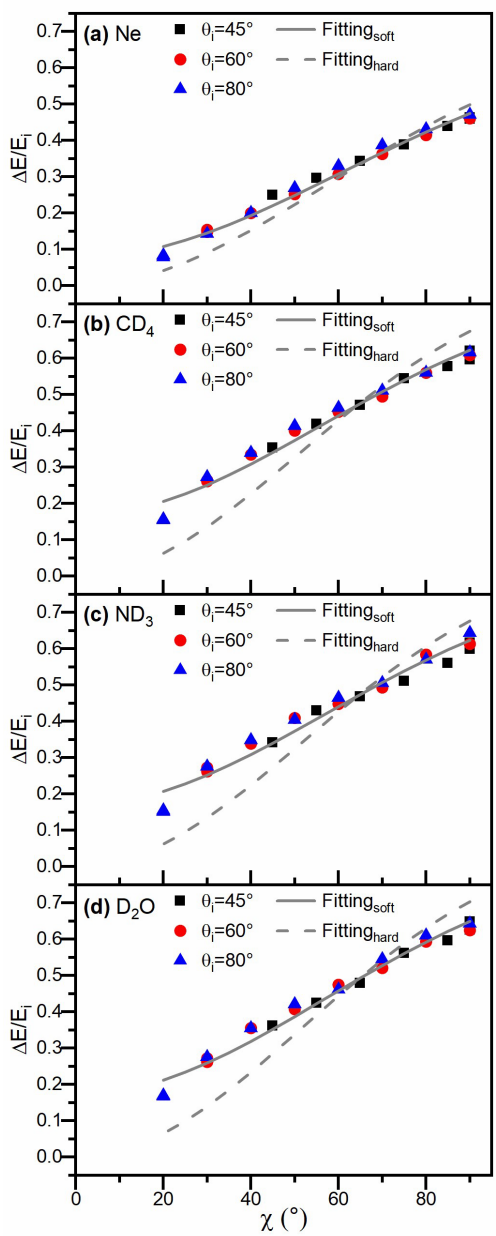

Figure 6. Average fractional energy loss as a function of deflection angle for impulsively scattered (a) Ne, (b) CD_4, (c) ND_3, and (d) D_2O from a dodecane flat jet. Incident translational energies are 23.7, 29.3, 28.8, and 33.4 kJ mol^{-1}, respectively. The solid curves give predictions for the soft-sphere model, where the incident particle interacts with a localized region of the surface with an effective mass, m_{eff}, and this region may increase its internal energy, E_{int}, during collisions. The dashed curves give predictions for the hard-sphere model where internal excitation has been set to zero. The fitting results for Ne, CD_4, ND_3, and D_2O with the soft-sphere model are m_{eff} = 61, 52, 55, and 54 amu and E_{int} = 2.1, 5.3, 5.1, and

5.8 kJ mol^{-1}, respectively, whereas the hard-sphere model predicts m_{eff} = 48, 34, 36, and 35 amu, respectively.

Fig. 6(a–d) shows the measured fractional translational energy loss plotted against deflection angle for scattering of Ne, CD_4, ND_3, and D_2O. The fractional energy loss increases with χ regardless of incidence angle for all four scatterers, consistent with observations made prior in the literature for other liquid surfaces.[35,71] For Ne, the fractional energy loss ranges from 0.15 to 0.46 between χ = 30° and 90°. For the polyatomic scatterers, D_2O energy loss increases from 0.27 to 0.64, while CD_4 and ND_3 behave similarly, with values ranging from 0.27 to 0.61 for both species. This trend of larger fractional energy losses for the polyatomic species compared to Ne at all values of χ is also present for the other two incidence angles chosen in this study.

The results of fitting the soft-sphere kinematic model to the fractional energy loss values are also shown in Fig. 6 alongside the hard-sphere model fits, where E_{int} is set to be zero. The free-fit parameters are m_{eff} and E_{int} where applicable, and V is set to a fixed value given by the well depths between the scatterers and dodecane. For both kinematic models, values of V for Ne, CD_4, ND_3, and D_2O are 0.9, 1.9, 2.8, and 3.6 kJ mol^{-1}, respectively.[75-78] If V is also set to be zero, assuming a completely noninteracting system, the best-fitted curves do not change to a significant degree. Inspecting the best-fit curves for the two models, the fractional energy loss behavior in the IS channel is best described by the soft-sphere kinematic model for all four scatterers. Due to the small value for E_{int} in the case of Ne, the hard-sphere and soft-sphere fits are more similar to one another compared to the fits for the polyatomic scatterers.

Table 1. Average fractional energy loss in the IS Channel at a deflection angle of $\chi = 90°$ and soft-sphere fitted parameters for all values of χ.

Scattered Species	Fractional Energy Loss $\Delta E/E_i$		Soft-Sphere Fitted Parameters	
	Dodecane	[a]Squalane	Effective Surface Mass m_{eff} (amu)	Total Internal Excitation E_{int} (kJ mol^{-1})
Ne	0.46	0.42	61	2.1
CD_4	0.61	[b]0.49	52	5.3
ND_3	0.62	[c]0.52	55	5.1
D_2O	0.64	0.56	54	5.8

[a]Gas scattering from liquid squalane. Values interpolated from Fig. 4 in ref. [51] to directly compare scattering at identical beam energies for each species. [b]Value reported for CH_4. [c]Value reported for NH_3.

Comparing these fractional energy loss values to literature values from squalane experiments at a fixed deflection angle of $\chi = 90°$,[51] we observe that the relative behavior between the four scatterers is similar for dodecane and squalane. The energy loss ordering for scattering from dodecane is Ne < CD_4 < ND_3 < D_2O, which agrees with the reported ordering of Ne < CH_4 < NH_3 < D_2O for scattering from squalane. These values can be found in Table 1.

At $\chi = 45$ and 90°, we observe fractional energy loss values of 0.25 and 0.46, respectively, for Ne scattered from dodecane. In a comparable study performed on a squalane surface,[35] fractional energy loss values of 0.36 and 0.58 were reported. Given that the incident beam energies were similar (*cf.* 23.7 kJ mol^{-1} in this work, 32 kJ mol^{-1} in ref. [35]), it is plausible that more internal modes within the squalane surface contribute to collision events compared to the dodecane surface, leading to the reduction in fractional energy loss. Thus, we conclude that squalane is a "softer," less rigid surface than dodecane. Further discussion on the relative rigidity between these two surfaces can be found in Section IVb.

The best-fit soft sphere curves result in recovered values for m_{eff} and E_{int} in the scattering of Ne, CD_4, ND_3, and D_2O, shown in Table 1. Given that the molecular mass of dodecane is ~170 amu, these results suggest that only a portion of any dodecane molecule contributes to fractional energy loss in the IS

channel, as the effective surface masses are about one-third of the dodecane mass. The polyatomic scatterers all exhibit similar values of E_{int}, contrasting with the smaller value for Ne scattering.

Examining the fitted values for the total internal excitation and considering that all four species have nearly identical masses and initial energies, the larger values for E_{int} that arise from molecular scattering compared to Ne scattering are likely due to the presence of internal degrees of freedom. It is plausible that rotational and vibrational modes may be excited, seen previously in gas–solid scattering.[79,80] However, we conclude that only rotational degrees of freedom contribute to the extracted values of E_{int} based on the relatively low values of E_{i} for all four beams and the maximum values of fractional energy loss occurring at $\chi = 90°$. As a result, the lowest lying vibrational modes[81] for CD_4, ND_3, and D_2O, ν_4 (11.9 kJ mol^{-1}), ν_2 (8.95 kJ mol^{-1}), and ν_2 (14.1 kJ mol^{-1}), respectively, are unlikely to be populated to a significant degree. It then follows that the differences in internal excitation values between Ne and CD_4, ND_3, and D_2O, 3.2, 3.0, and 3.7 kJ mol^{-1}, respectively, correspond to the rotational energies of the scattered molecules.

IVb. DISCUSSION OF THERMAL DESORPTION FROM DODECANE

The TD fraction derived from the $\theta_{\mathrm{i}} = 60°$ scattering angular distributions, defined as TD/(TD+IS), is plotted in Fig. 7 for Ne, CD_4, ND_3, and D_2O as a function of deflection angle. All four scatterers exhibit increasing TD fractions as χ increases, except for a slight deviation in the case of Ne scattering at $\chi = 30°$. It is observed that Ne scattering results in the smallest TD fractions at all values of χ while, for the most part, the polyatomic molecules behave similarly.

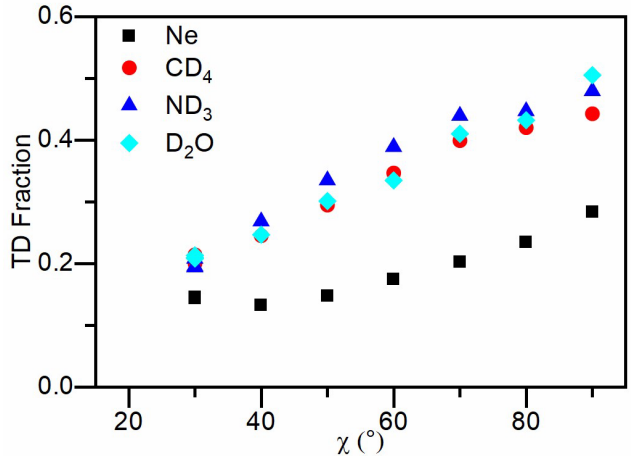

Figure 7. TD fraction as a function of deflection angle for Ne, CD_4, ND_3, and D_2O scattered from a dodecane flat jet at $\theta_i = 60°$.

At a fixed incidence angle, the increasing TD fraction with increasing deflection angle is expected since a larger value of χ corresponds to collisions where more momentum normal to the surface has been lost from the projectile. This trend is also seen for both $\theta_i = 45$ and 80°. Additional factors must be considered to explain why the Ne trend is so different than that of the polyatomic scatterers. For example, the uptake of incidence energy in internal degrees of freedom may correlate with χ or the trapping well depth for Ne may be significantly smaller than for the polyatomic scatterers.

Overall, the observed TD fraction trend of $ND_3 > D_2O \approx CD_4 > Ne$ follows that which has been reported for scattering from squalane at similar beam energies at a single deflection angle $\chi = 90°$.[51] As has been previously pointed out for scattering from squalane, the TD fraction correlates with the projectiles' free energies of solvation ($\Delta G^{\circ}_{\mathrm{solv}} = -RT \ln K_{\mathrm{H}}$).[51] In comparing the TD fraction values for CD_4 (0.40), ND_3 (0.49), and D_2O (0.48) scattered from dodecane with the analogous values for CH_4 (0.49), NH_3 (0.59), and D_2O (0.57) scattered from squalane (interpolated from ref. [51] on the basis of beam energy), we see that scattering from dodecane leads to TD fractions ca. 17% smaller than those for squalane scattering. Thus, collisions undergone by these polyatomic scatterers are harder with dodecane, indicating that it is a more rigid surface.

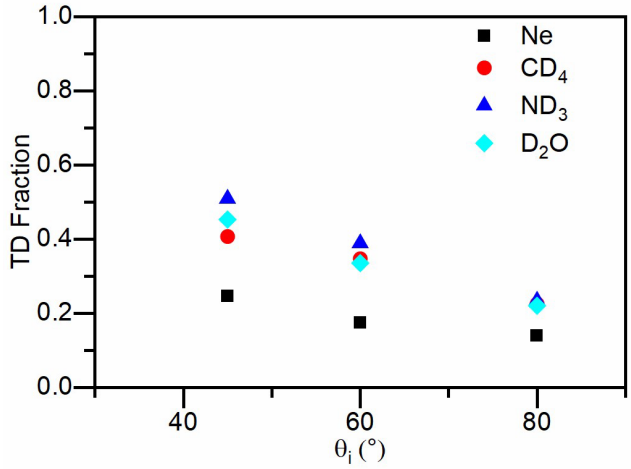

Figure 8. TD fraction at $\theta_f = 60°$ as a function of incidence angle for Ne, CD_4, ND_3, and D_2O scattered from a dodecane flat jet.

The dependence of TD fraction on incidence angle is shown in Fig. 8 for the four scatterers. Here, the TD fraction trend of $ND_3 > D_2O \approx CD_4 > Ne$ is seen again. The TD fraction decreases as θ_i increases, as has been seen in other gas–liquid scattering experiments.[35,82,83] Interestingly, this trend is opposite to that observed in gas–solid scattering experiments.[84-87] Nesbitt[83] has attributed this difference to the increase roughness and corrugation of a liquid surface compared to a single crystal solid surface, leading to the conversion of incident kinetic energy in high θ_i collisions into translational motion away from the liquid surface.

V. EVAPORATION AND SCATTERING FROM COLD SALTY WATER

Initial experiments have been performed on the evaporation and scattering of Ar ($E_i = 41.5$ kJ mol^{-1}) from a flat jet of cold salty water, using the instrument shown in Fig. 1. Using a similar strategy to that described above for dodecane, we first characterized the TD channel by observing the evaporation of Ar from an Ar-doped salty water jet. Fig. 9 (a) shows the resultant TOF spectra at $\theta_f = 0$, 30, and 60°.

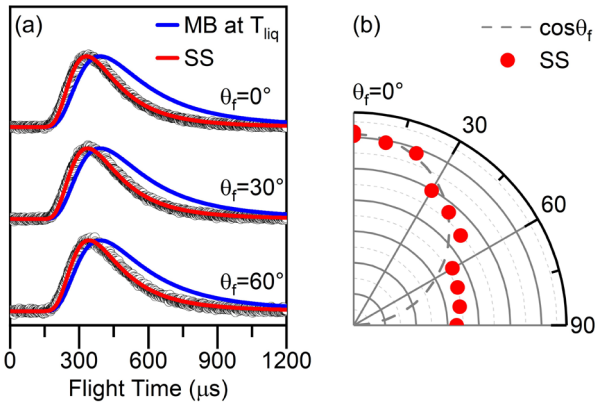

Figure 9. (a) Normalized evaporation TOF spectra of Ar from an Ar-doped aqueous LiBr flat jet at $\theta_f = 0$, 30, and 60°. TOF distributions are fitted by an SS distribution (red traces); an MB distribution (blue traces) at T_{liq} = 226 K is shown for comparison. (b) Angular plot created from the integrated, non-normalized intensities of the SS simulations (red circles) at various detector angles. The cosine function representing the expected angular distribution for evaporation is indicated by the dashed gray curve.

The TOF spectra reflect Ar velocity distributions that are slightly faster than those of a thermal distribution at the temperature of the liquid, shown as a blue trace. This super-Maxwellian character may indicate that Ar–H_2O collisions are occurring in the gas-phase above the surface, accelerating the Ar atoms in a kind of supersonic expansion. However, other explanations are possible. If the sticking probability of Ar is enhanced by incidence translational energy, for example due to a barrier associated with solvent reorganization as has been seen for He/H_2O,[88] detailed balance tells us that evaporating Ar atoms will be emitted with velocities faster than the Boltzmann expectation. For this system, this is unlikely as prior studies have shown that Ar evaporation from cold salty water is Maxwellian.[46] An angular plot of the integrated TOF fits shown in Fig. 9 (b) reveals that evaporation from the jet surface deviates from a $\cos\theta_f$ distribution (dashed gray curve). Given these observations, there likely exists a constant, isotropic background signal emanating from the cryogenically cooled Cu wall in analogy to the dodecane studies.[49,50]

Exploratory measurements were performed on Ar scattering from an aqueous LiBr jet. The resultant TOF spectrum is shown in Fig. 10.

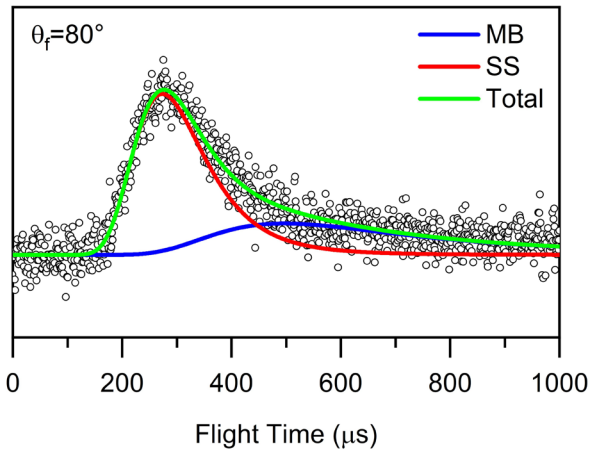

Figure 10. TOF spectrum of Ar scattering from a salty water flat jet with $\theta_i = 60°$ at $\theta_f = 80°$. The data is fitted by the sum of an SS distribution (red trace) and an MB distribution (blue trace) at the liquid jet temperature. The sum of the two contributions is shown by the green trace.

From the integrated fits, a TD fraction of 0.23 is extracted. In comparison to the values measured for particles scattered from dodecane at the same geometry ($\theta_i = 60°$, $\theta_f = 80°$, $\chi = 40°$), this result suggests that Ar has a lower proclivity for impulsive scattering from cold salty water than Ne does from dodecane, but is more prone to IS than CD_4, ND_3, and D_2O from dodecane. While the free energy of solvation successfully describes the trend in TD fraction of the dodecane scatterers, extending this comparison to Ar scattering is nontrivial. To the best of our knowledge, $\Delta G^{\circ}_{\mathrm{solv}}$ for Ar in 8 m LiBr has not been measured, and extrapolation from reference data provides only a rough estimate of ca. 39 kJ mol^{-1}, which lies far outside the range of values reported for the dodecane scatterers.[89] Additionally, the mean translational energy of the Ar molecular beam is between 25 and 75% larger than that of the dodecane scattering partners. This results in higher collisional energies and likely plays a role in the relative TD fractions observed for different gas–liquid systems. Further studies are currently underway to characterize and understand the scattering behavior of Ar from a cold salty water jet.

VI. CONCLUSIONS

In this work, we review recent progress in molecular scattering experiments from a volatile flat liquid jet to determine how scatterer and liquid identity affects scattering and energy transfer at the gas–liquid interface. We have reported results on the evaporation of Ne, CD_4, ND_3, and D_2O from doped dodecane

jets along with the scattering of these four species from pure dodecane jets, as well as evaporation and scattering of Ar from cold salty water jets. The combination of well-defined angular distributions from the flat jet and time-of-flight measurements that characterize the translational energy of the scatterers provides a fundamental understanding of the gas–liquid interface from a mechanistic perspective.

The dodecane evaporation TOF profiles for all four species are best described by an MB flux distribution at T_{liq} after background subtraction and exhibit $\cos\theta_{\mathrm{f}}$ angular distributions characteristic of evaporation from a flat surface and a sticking coefficient of unity. In the scattering experiments, the scattering TOF spectra for all four scatterers are fitted by a linear combination of a faster IS component and a slower TD component. Integrating these spectra results in super-specular scattering in the IS channel, attributed to anisotropic momentum transfer at the interface, and $\cos\theta_{\mathrm{f}}$ angular distributions for the TD channel.

In the IS channel, the fractional energy loss is smallest for Ne and largest for D_2O. This trend was also found in prior squalane scattering experiments, but the fractional energy loss from dodecane is smaller than from squalane. This shows that squalane is a softer surface than dodecane.

The TD fraction is largest for collision trajectories with a larger deflection angle and smallest for grazing trajectories. CD_4, ND_3, and D_2O scattering resulted in similar TD fractions, contrasting with Ne scattering. The relative TD fractions correlate with free energies of solvation in dodecane, consistent with the prior literature. These findings showcase the importance of collision geometry and scatterer identity toward the likelihood of being trapped at the interface. We then applied a soft-sphere kinematic model to describe energy loss in the impulsive mechanistic channel. CD_4, ND_3, and D_2O exhibit larger values for internal excitation than Ne, attributed to rotational excitation of the polyatomic scatterers.

The salty water experiments indicated that Ar atoms evaporating from a jet of 8 m LiBr undergo collisions with water vapor above the surface of the jet, resulting in TOF distributions that are slightly super-Maxwellian. Initial results from Ar scattering experiments suggest that Ar is more likely to undergo surface trapping by cold salty water than Ne is on dodecane, but less so than the molecular scatterers from dodecane.

We have elucidated interfacial interactions by probing atomic and molecular scattering dynamics at the gas–liquid interface using a flat liquid jet. This work will serve as a useful benchmark for studying future volatile solvent systems including aqueous media. We plan to continue to investigate nonreactive and reactive scattering from a cold salty water flat jet. Preliminary results are presented here, and further experiments are currently underway, supported by the framework established in this body of work.

AUTHOR INFORMATION

Corresponding Author

Daniel M. Neumark − *Department of Chemistry, University of California, Berkeley, CA 94720, USA*; *Chemical Sciences Division, Lawrence Berkeley National Laboratory, Berkeley, CA 94720, USA*; https://orcid.org/0000-0002-3762-9473; Email: dneumark@berkeley.edu

Authors

Walt Yang − *Department of Chemistry, University of California, Berkeley, CA 94720, USA*; *Chemical Sciences Division, Lawrence Berkeley National Laboratory, Berkeley, CA 94720, USA*; https://orcid.org/0000-0003-4296-3801

Madison M. Foreman − *Department of Chemistry, University of California, Berkeley, CA 94720, USA*; *Chemical Sciences Division, Lawrence Berkeley National Laboratory, Berkeley, CA 94720, USA*; https://orcid.org/0000-0002-6516-5426

Steven Saric – *Department of Chemistry, University of California, Berkeley, CA 94720, USA*; *Chemical Sciences Division, Lawrence Berkeley National Laboratory, Berkeley, CA 94720, USA*; https://orcid.org/0009-0005-5135-8875

Alec M. Wodtke − *Department of Dynamics at Surfaces, Max Planck Institute for Multidisciplinary Sciences, am Faßberg 11, 37077 Göttingen, Germany*; *Institute for Physical Chemistry, Georg-August University of Göttingen, Tammannstraße 6, 37077 Göttingen, Germany*; https://orcid.org/0000-0002-6509-2183

Kevin R. Wilson – *Chemical Sciences Division, Lawrence Berkeley National Laboratory, Berkeley, CA 94720, USA*; https://orcid.org/0000-0003-0264-0872

Current Addresses

Steven Saric – *Diablo Valley College, Pleasant Hill, CA 94523*

Author Contributions

Walt Yang: Conceptualization (equal); Data curation (lead); Formal analysis (lead); Investigation (lead); Methodology (equal); Software (equal); Writing – original draft (lead); Writing – review & editing (equal).

Madison M. Foreman: Conceptualization (supporting); Data curation (supporting); Formal analysis (supporting); Investigation (supporting); Methodology (supporting); Software (supporting); Writing – original draft (supporting); Writing – review & editing (equal).

Steven Saric: Investigation (supporting); Methodology (supporting); Writing – review & editing (supporting).

Alec M. Wodtke: Investigation (supporting); Methodology (supporting); Project administration (supporting); Supervision (supporting); Validation (supporting); Writing – review & editing (equal).

Kevin R. Wilson: Methodology (supporting); Project administration (supporting); Resources (equal); Supervision (supporting); Validation (supporting); Writing – review & editing (equal).

Daniel M. Neumark: Conceptualization (lead); Methodology (equal); Project administration (lead); Resources (lead); Supervision (lead); Validation (lead); Writing – review & editing (equal).

ACKNOWLEDGMENTS

The authors acknowledge the support by the Office of Basic Energy Science, Chemical Sciences Division of the U.S. Department of Energy under Contract No. DE-AC02-05CH11231. A.M.W. acknowledges support from the Miller Institute for Basic Research in Science at the University of California, Berkeley through the Gabor A. and Judith K. Somorjai Visiting Miller Professorship Award. The authors thank Chin Lee and Marvin Pohl for their contributions to the development of the salty water experiments. The authors thank Bernd Winter, Bernd Abel, and Manfred Faubel for helpful discussions in the early phases of this work.

AUTHOR DECLARATIONS

Conflict of Interest

The authors declare no conflicts of interest.

DATA AVAILABILITY

The data that support the findings of this study are available from the corresponding author upon reasonable request.

REFERENCES

1. Uppu RM, Cueto R, Squadrito GL, Pryor WA. What Does Ozone React with at the Air Lung Interface? Model Studies Using Human Red Blood Cell Membranes. *Arch Biochem Biophys*. 1995;319(1):257–266.
2. Sosnowski TR, Kubski P, Wojciechowski K. New experimental model of pulmonary surfactant for biophysical studies. *Colloids Surf A*. 2017;519:27-33.
3. Wallington TJ, Kaiser EW, Farrell JT. Automotive fuels and internal combustion engines: a chemical perspective. *Chem Soc Rev*. 2006;35(4):335.
4. Littel R, Van Swaaij WPM, Versteeg GF. Kinetics of carbon dioxide with tertiary amines in aqueous solution. *AIChE J*. 1990;36(11):1633-1640.
5. Dentener FJ, Crutzen PJ. Reaction of N_2O_5 on tropospheric aerosols: Impact on the global distributions of NO_x, O_3, and OH. *Journal of Geophysical Research: Atmospheres*. 1993;98(D4):7149-7163.
6. Singh A, Agrawal M. Acid rain and its ecological consequences. *J Environ Biol*. 2008;29:15–24.
7. Donaldson D, Valsaraj KT. Adsorption and reaction of trace gas-phase organic compounds on atmospheric water film surfaces: A critical review. *Environmental science & technology*. 2010;44(3):865-873.
8. Putikam R, Lin M-C. A novel mechanism for the isomerization of N_2O_4 and its implication for the reaction with H_2O and acid rain formation. *Int J Quantum Chem*. 2018;118(12):e25560.
9. Ruiz-López MF, Martins-Costa MTC, Anglada JM, Francisco JS. A New Mechanism of Acid Rain Generation from HOSO at the Air–Water Interface. *J Am Chem Soc*. 2019;141(42):16564–16568.
10. Gao X-F, Nathanson GM. Exploring Gas-Liquid Reactions with Microjets: Lessons We Are Learning. *Acc Chem Res*. 2022;55:3294-3302.

11. Nesbitt DJ, Zolot AM, Roscioli JR, Ryazanov M. Nonequilibrium Scattering/Evaporation Dynamics at the Gas-Liquid Interface: Wetted Wheels, Self-Assembled Monolayers, and Liquid Microjets. *Acc Chem Res*. 2023;56:700-711.

12. Devlin SW, Bernal F, Riffe EJ, Wilson KR, Saykally RJ. Spiers Memorial Lecture: Water at interfaces. *Faraday Disc*. 2023;

13. Richmond GL. Molecular Bonding and Interactions at Aqueous Surfaces as Probed by Vibrational Sum Frequency Spectroscopy. *Chem Rev*. 2002;102(8):2693–2724.

14. McGuire JA, Shen YR. Ultrafast Vibrational Dynamics at Water Interfaces. *Science*. 2006;313:1945–1948.

15. Petersen PB, Saykally RJ. On the Nature Of Ions at the Liquid Water Surface. *Annu Rev Phys Chem*. 2006;57(1):333–364.

16. Rizzuto AM, Irgen-Gioro S, Eftekhari-Bafrooei A, Saykally RJ. Broadband Deep UV Spectra of Interfacial Aqueous Iodide. *J Phys Chem Lett*. 2016/10/06 2016;7(19):3882-3885.

17. Mizuno H, Rizzuto AM, Saykally RJ. Charge-Transfer-to-Solvent Spectrum of Thiocyanate at the Air/Water Interface Measured by Broadband Deep Ultraviolet Electronic Sum Frequency Generation Spectroscopy. *J Phys Chem Lett*. 2018/08/16 2018;9(16):4753-4757.

18. Bhattacharyya D, Mizuno H, Rizzuto AM, Zhang Y, Saykally RJ, Bradforth SE. New Insights into the Charge-Transfer-to-Solvent Spectrum of Aqueous Iodide: Surface versus Bulk. *J Phys Chem Lett*. 2020;11(5):1656-1661.

19. Mizuno H, Oosterbaan KJ, Menzl G, et al. Revisiting the $\pi \rightarrow \pi^*$ transition of the nitrite ion at the air/water interface: A combined experimental and theoretical study. *Chem Phys Lett*. 2020/07/16/ 2020;751:137516.

20. Yu C-C, Seki T, Chiang K-Y, et al. Polarization-Dependent Heterodyne-Detected Sum-Frequency Generation Spectroscopy as a Tool to Explore Surface Molecular Orientation and Ångström-Scale Depth Profiling. *J Phys Chem B*. 2022/08/25 2022;126(33):6113-6124.

21. Li Y, Yan X, Cooks RG. The Role of the Interface in Thin Film and Droplet Accelerated Reactions Studied by Competitive Substituent Effects. *Angew Chem Int Ed*. 2016;55(10):3433–3437.

22. Nam I, Lee JK, Nam HG, Zare RN. Abiotic production of sugar phosphates and uridine ribonucleoside in aqueous microdroplets. *PNAS*. 2017;114(47):12396–12400.

23. Diveky ME, Gleichweit MJ, Roy S, Signorell R. Shining New Light on the Kinetics of Water Uptake by Organic Aerosol Particles. *J Phys Chem A*. 2021;125(17):3528–3548.

24. Wokosin KA, Schell EL, Faust JA. Emerging investigator series: surfactants, films, and coatings on atmospheric aerosol particles: a review. *Environmental Science: Atmospheres*. 2022;2(5):775-828.

25. Weinberg WH. Molecular beam scattering from solid surfaces. *Adv Colloid Interface Sci*. 1975;4:301–347.

26. Hurst JE, Becker CA, Cowin JP, Janda KC, Wharton L, Auerbach DJ. Observation of Direct Inelastic Scattering in the Presence of Trapping-Desorption Scattering: Xe on Pt(111). *Phys Rev Lett*. 1979;43(16):1175–1177.

27. Barker JA, Auerbach DJ. Gas—surface interactions and dynamics; Thermal energy atomic and molecular beam studies. *Surf Sci Rep*. 1984;4(1-2):1-99.

28. Harten U, Lahee AM, Toennies JP, Wöll C. Observation of a Soliton Reconstruction of Au(111) by High-Resolution Helium-Atom Diffraction. *Phys Rev Lett*. 1985;54(24):2619-2622.

29. Huang Y, Rettner CT, Auerbach DJ, Wodtke AM. Vibrational Promotion of Electron Transfer. *Science*. 2000;290(5489):111-114.

30. Faubel M, Schlemmer S, Toennies JP. A molecular beam study of the evaporation of water from a liquid jet. *Z Phys D Atoms, Molecules and Clusters*. 1988;10(2-3):269–277.

31. Faubel M, Kisters T. Non-equilibrium molecular evaporation of carboxylic acid dimers. *Nature*. 1989;339(6225):527–529.

32. Ekimova M, Quevedo W, Faubel M, Wernet P, Nibbering ETJ. A liquid flatjet system for solution phase soft-x-ray spectroscopy. *Structural Dynamics*. 2015;2(5):054301.

33. Lednovich SL, Fenn JB. Absolute evaporation rates for some polar and nonpolar liquids. *AIChE Journal*. 1977;23(4):454–459.

34. Siegbahn H. Electron spectroscopy for chemical analysis of liquids and solutions. *J Phys Chem*. 1985;89(6):897–909.

35. King ME, Nathanson GM, Hanning-Lee M, Minton TK. Probing the microscopic corrugation of liquid surfaces with gas–liquid collisions. *Phys Rev Lett*. 1993;70(7):1026–1029.

36. Nathanson GM, Davidovits P, Worsnop DR, Kolb CE. Dynamics and Kinetics at the Gas−Liquid Interface. *J Phys Chem*. 1996;100(31):13007–13020.

37. Wu B, Zhang J, Minton TK, et al. Scattering Dynamics of Hyperthermal Oxygen Atoms on Ionic Liquid Surfaces: [emim][NTf_2] and [C_{12}mim][NTf_2]. *J Phys Chem C*. 2010;114(9):4015–4027.

38. Brastad SM, Nathanson GM. Molecular beam studies of HCl dissolution and dissociation in cold salty water. *Phys Chem Chem Phys*. 2011;13(18):8284.

39. Lancaster DK, Johnson AM, Burden DK, Wiens JP, Nathanson GM. Inert Gas Scattering from Liquid Hydrocarbon Microjets. *J Phys Chem Lett*. 2013;4(18):3045–3049.

40. Faust JA, Sobyra TB, Nathanson GM. Gas–Microjet Reactive Scattering: Collisions of HCl and DCl with Cool Salty Water. *J Phys Chem Lett*. 2016;7(4):730–735.

41. Shaloski MA, Gord JR, Staudt S, Quinn SL, Bertram TH, Nathanson GM. Reactions of N_2O_5 with Salty and Surfactant-Coated Glycerol: Interfacial Conversion of Br^- to Br_2 Mediated by Alkylammonium Cations. *J Phys Chem A*. 2017;121(19):3708–3719.

42. Sobyra TB, Melvin MP, Nathanson GM. Liquid Microjet Measurements of the Entry of Organic Acids and Bases into Salty Water. *J Phys Chem C*. 2017;121(38):20911–20924.

43. Gord JR, Zhao X, Liu E, Bertram TH, Nathanson GM. Control of Interfacial Cl_2 and N_2O_5 Reactivity by a Zwitterionic Phospholipid in Comparison with Ionic and Uncharged Surfactants. *J Phys Chem A*. 2018;122(32):6593–6604.

44. Lane PD, Moncrieff KE, Greaves SJ, McKendrick KG, Costen ML. Inelastic Scattering of CN Radicals at the Gas–Liquid Interface Probed by Frequency-Modulated Absorption Spectroscopy. *J Phys Chem C*. 2020;124(30):16439–16448.

45. Saecker ME, Govoni ST, Kowalski DV, King ME, Nathanson GM. Molecular Beam Scattering from Liquid Surfaces. *Science*. 1991;252:1421–1424.

46. Faust JA, Nathanson GM. Microjets and coated wheels: versatile tools for exploring collisions and reactions at gas–liquid interfaces. *Chem Soc Rev*. 2016;45(13):3609–3620.

47. Koralek JD, Kim JB, Brůža P, et al. Generation and characterization of ultrathin free-flowing liquid sheets. *Nat Commun*. 2018;9(1)

48. Lee C, Pohl MN, Ramphal IA, et al. Evaporation and Molecular Beam Scattering from a Flat Liquid Jet. *J Phys Chem A*. 2022;126(21):3373–3383.

49. Yang W, Lee C, Saric S, Pohl MN, Neumark DM. Evaporation and scattering of neon, methane, and water from a dodecane flat liquid jet. *J Chem Phys*. 2023;159(5)

50. Saric S, Yang W, Neumark DM. Molecular Beam Scattering of Ammonia from a Dodecane Flat Liquid Jet. *Faraday Disc*. 2024, accepted;

51. Saecker ME, Nathanson GM. Collisions of protic and aprotic gases with hydrogen bonding and hydrocarbon liquids. *J Chem Phys*. 1993;99(9):7056–7075.

52. Kinefuchi I, Yamaguchi H, Shiozaki S, Sakiyama Y, Matsumoto Y. Out-of-plane Scattering Distribution of Nitrogen Molecular Beam on Graphite (0001) Surface. *AIP Conf Proc*. 2005;762(947)

53. Tesa-Serrate MA, Smoll EJ, Minton TK, McKendrick KG. Atomic and Molecular Collisions at Liquid Surfaces. *Annu Rev Phys Chem*. 2016;67(1):515–540.

54. Sobyra TB, Pliszka H, Bertram TH, Nathanson GM. Production of Br_2 from N_2O_5 and Br^- in Salty and Surfactant-Coated Water Microjets. *J Phys Chem A*. 2019/10/17 2019;123(41):8942-8953.

55. Lee YT, McDonald JD, Lebreton PR, Herschbach DR. Molecular Beam Reactive Scattering Apparatus with Electron Bombardment Detector. *Rev Sci Instrum*. 1969;40(11):1402–1408.

56. Lee YT. Molecular Beam Studies of Elementary Chemical Processes (Nobel Lecture). *Angew Chem Int Ed Engl*. 1987;26(10):939–951.

57. Irimia D, Dobrikov D, Kortekaas R, et al. A short pulse (7 μs FWHM) and high repetition rate (dc-5kHz) cantilever piezovalve for pulsed atomic and molecular beams. *Rev Sci Instrum*. 2009;80(11):113303.

58. Meng C, Janssen MHM. Measurement of the density profile of pure and seeded molecular beams by femtosecond ion imaging. *Rev Sci Instrum*. 2015;86(2):023110.

59. Sasse K, Jose J, Merlin JC. A static apparatus for measurement of low vapor pressures. Experiment results on high molecular-weight hydrocarbons. *Fluid Phase Equilib*. 1988;42:287–304.

60. Lemmon EW, Huber ML. Thermodynamic Properties of *n*-Dodecane. *Energy Fuels*. 2004;18(4):960–967.

61. Comsa G, David R. Dynamical parameters of desorbing molecules. *Surf Sci Rep*. 1985;5:145–198.

62. Day C. In: Brandt D, ed. *CAS—CERN Accelerator School: Vacuum in Accelerators*. CERN; 2007:241–274.

63. Brenig W. Dynamics and kinetics of gas-surface interaction: Sticking, desorption and inelastic scattering. *Phys Scr*. 1987;35(3):329.

64. Kennard EH. *Kinetic Theory of Gases*. McGraw-Hill Book Company; 1938.

65. Kann ZR, Skinner JL. Sub- and super-Maxwellian evaporation of simple gases from liquid water. *J Chem Phys*. 2016;144(15):154701.

66. Morse MD. In: Dunning FB, Hulet RG, eds. *Atomic, Molecular, and Optical Physics: Atoms and Molecules*. Academic Press; 1996:21–47.

67. Lebehot A, Kurzyna J, Lago V, Dudeck M, Campargue R. In: Campargue R, ed. *Atomic and Molecular Beams*. Springer; 2001:237–251.

68. Kinefuchi I, Kotsubo Y, Osuka K, et al. Incident energy dependence of the scattering dynamics of water molecules on silicon and graphite surfaces: the effect on tangential momentum accommodation. *Microfluidics and Nanofluidics*. 2017;21(2)

69. Subbarao RB, Miller DR. Velocity distribution measurements of 0.06–1.4 eV argon and neon atoms scattered from the (111) plane of a silver crystal. *J Chem Phys*. 1973;58(12):5247-5257.

70. Rettner CT, Delouise LA, Auerbach DJ. Effect of incidence kinetic energy and surface coverage on the dissociative chemisorption of oxygen on W(110). *J Chem Phys*. 1986;85(2):1131-1149.

71. Alexander WA, Zhang J, Murray VJ, Nathanson GM, Minton TK. Kinematics and dynamics of atomic-beam scattering on liquid and self-assembled monolayer surfaces. *Faraday Disc*. 2012;157:355.

72. Andric N, Jenny P. Molecular dynamics investigation of energy transfer during gas-surface collisions. *Phys Fluids*. 2018;30(7):077104.

73. Rettner CT, Ashfold MNR. *Dynamics of Gas-Surface Interactions*. Royal Society of Chemistry; 1991.

74. Nathanson GM. Molecular Beam Studies of Gas–Liquid Interfaces. *Annu Rev Phys Chem*. 2004;55(1):231–255.

75. Lorentz HA. Ueber die Anwendung des Satzes vom Virial in der kinetischen Theorie der Gase. *Annalen der Physik*. 1881;248(1):127–136.

76. Berthelot D. Sur le mélange des gaz. *Comptes rendus hebdomadaires des séances de l'Académie des Sciences*. 1898;126:1703–1855.

77. Mourits FM, Rummens FHA. A critical evaluation of Lennard-Jones and Stockmayer potential parameters and of some correlation methods. *Can J Chem*. 1977;55(16):3007–3020.

78. Chen C-K, Banaszak M, Radosz M. Statistical Associating Fluid Theory Equation of State with Lennard-Jones Reference Applied to Pure and Binary *n*-Alkane Systems. *J Phys Chem B*. 1998;102(13):2427–2431.

79. Rettner C, Fabre F, Kimman J, Auerbach D. Observation of direct vibrational excitation in gas-surface collisions: NO on Ag (111). *Phys Rev Lett*. 1985;55(18):1904.

80. Kay BD, Raymond T, Coltrin ME. Observation of Direct Multiquantum Vibrational Excitation in Gas-Surface Scattering: NH_3 on Au (111). *Phys Rev Lett*. 1987;59(24):2792.

81. Shimanouchi T. *Tables of molecular vibrational frequencies*. vol 1. National Bureau of Standards Washington, DC; 1972.

82. King ME, Fiehrer KM, Nathanson GM, Minton TK. Effects of Thermal Roughening on the Angular Distributions of Trapping and Scattering in Gas−Liquid Collisions. *J Phys Chem A*. 1997;101(36):6556-6561.

83. Perkins BG, Nesbitt DJ. Toward Three-Dimensional Quantum State-Resolved Collision Dynamics at the Gas−Liquid Interface: Theoretical Investigation of Incident Angle. *J Phys Chem A*. 2009;113(16):4613-4625.

84. Mullins CB, Rettner CT, Auerbach DJ, Weinberg WH. Variation of the trapping probability of Ar on Pt(111) with kinetic energy and angle of incidence: The changing role of parallel momentum with surface temperature. *Chem Phys Lett*. 1989;163(2–3):111-115.

85. Rettner CT, Mullins CB, Bethune DS, Auerbach DJ, Schweizer EK, Weinberg WH. Molecular beam studies of trapping dynamics. *J Vac Sci Technol A*. 1990;8:2699-2704.

86. Head-Gordon M, Tully JC, Rettner CT, Mullins CB, Auerbach DJ. On the nature of trapping and desorption at high surface temperatures. Theory and experiments for the Ar–Pt(111) system. *J Chem Phys*. 1991;94(2):1516–1527.

87. Rettner CT, Kimman J, Auerbach DJ. Inelastic scattering of NO from Ag(111): Internal state, angle, and velocity resolved measurements. *J Chem Phys*. 1991;94:734-750.

88. Hahn C, Kann ZR, Faust JA, Skinner J, Nathanson GM. Super-Maxwellian helium evaporation from pure and salty water. *J Chem Phys*. 2016;144(4)

89. Hamme RC, Emerson SR. The solubility of neon, nitrogen and argon in distilled water and seawater. *Deep Sea Research Part I: Oceanographic Research Papers*. 2004;51(11):1517-1528.